Computer-Aided Design 43 (2011) 1427–1437

Contents lists available at SciVerse ScienceDirect

Computer-Aided Design

journal homepage: www.elsevier.com/locate/cad

Isogeometric analysis and shape optimization via boundary integral

Kang Li, Xiaoping Qian *

Department of Mechanical, Materials and Aerospace Engineering, Illinois Institute of Technology, Chicago, IL 60616, USA

ARTICLE INFO

Keywords:
Isogeometric analysis
Shape optimization
NURBS
CAD
Boundary integral

ABSTRACT

In this paper, we present a boundary integral based approach to isogeometric analysis and shape optimization.

For analysis, it uses the same basis, Non-Uniform Rational B-Spline (NURBS) basis, for both representing object boundary and for approximating physical fields in analysis via a Boundary-Integral-Equation Method (BIEM). We propose the use of boundary points corresponding to Greville abscissae as collocation points. We conducted h-, p- and k-refinement study for linear elasticity and heat conduction problems. Our numerical experiments show that collocation at Greville abscissae leads to overall better convergence and robustness. Replacing rational B-splines with the linear B-Splines as shape functions for approximating solution space in analysis does not yield significant difference in convergence.

For shape optimization, it uses NURBS control points to parameterize the boundary shape. A gradient based optimization approach is adopted where analytical sensitivities of how control points affect objective and constraint functions are derived. Two 3D shape optimization examples are demonstrated.

Our study finds that the boundary integral based isogeometric analysis and optimization have the following advantages: (1) the NURBS based boundary integral exhibits superior computational advantages over the usual Lagrange polynomials based BIEM on a per degree-of-freedom basis; (2) it bypasses the need for domain parameterization, a bottleneck in current NURBS based volumetric isogeometric analysis and shape optimization; (3) it offers tighter integration of CAD and analysis since both the geometric models for both analysis and optimization are the same NURBS geometry.

1. Introduction

Isogeometric analysis is a computational technique that uses the same basis to represent geometry and to approximate physical fields in analysis [1]. It has gathered growing interest from both analysis and CAD research communities due to its computational advantage over traditional finite element analysis and its promise to alleviate the burden of creating analysis-ready geometric models from the CAD representation. It has been successfully extended to a variety of boundary value problems [2].

To leverage the possible advantages of closer integration of CAD and FEA in isogeometric analysis and to utilize NURBS's capability of concise representation of complex shape, NURBS based isogeometric analysis has been extended to shape optimization where both NURBS control points [3–5] and weights [6] have been used as design variables to control the boundary shape.

However, a critical challenge remains in current isogeometric analysis and shape optimization practices. That is how to parameterize a volumetric domain from its boundary and it is referred to as domain parameterization in this paper. This is because that current isogeometric analysis approach [2] is based on a volumetric formulation where trivariate NURBS solids are needed for the analysis of three-dimensional (3D) problems while CAD systems use a boundary representation where only a surface representation is available. The creation of NURBS geometry that is amenable to isogeometric analysis has been referred to as "analysis-aware modeling" [7]. Methods such as lofting [8], swept volume parameterization [9], and discrete harmonic functions based techniques [10] have been proposed for domain parameterization. A Coons patch based method for constructing NURBS mesh from its boundary for isogeometric shape optimization has been proposed in [4].

This paper presents a new approach to isogeometric analysis and shape optimization that can bypass the need for domain parameterization. It is based on a boundary integral formulation of the analysis problem where the governing equations are transformed into integral equations on a boundary via the fundamental solutions of the underlying physical problems. The object boundary in the NURBS representation is discretized, without approximation, into many elements. The physical fields such as displacements and tractions in elasticity are approximated by NURBS. The integral equations are then converted to a set of linear equations from which the unknowns are solved. It should be noted that the idea of converting volumetric integral

* Corresponding author. Tel.: +1 312 567 5855.
E-mail addresses: kli@iit.edu (K. Li), qian@iit.edu (X. Qian).

0010-4485/$ – see front matter © 2011 Elsevier Ltd. All rights reserved.
doi:10.1016/j.cad.2011.08.031

to boundary integral to improve numerical accuracy and utilizing the geometric exactness in the NURBS representation for physical analysis has been explored in [11,12] where van der Waals forces between objects are computed. The idea of developing boundary integral based isogeometric analysis has been suggested in [1,2] and attempted in [13] for solving an external potential flow problem. Although NURBS based shape optimization via boundary integral has been explored in [14], it only used NURBS to represent the design boundary, not to approximate the physical fields for analysis. Further, the analytical gradients were not derived since it used evolutionary optimization.

Our study finds that the proposed approach, isogeometric analysis and shape optimization via boundary integral, has several advantages over existing analysis and optimization methods. They include: (1) geometric exactness from design representation to analysis model, (2) computational advantages over Lagrange polynomials based analysis on a per degree-of-freedom (DOF) basis, (3) bypassing the need for domain parameterization that is otherwise needed in the volumetric isogeometric analysis. The contributions of this paper include the following:

- A *boundary integral based isogeometric analysis* method has been developed. This includes all the essential steps in applying NURBS basis functions in the boundary integral process and the techniques for resolving singularities in kernel integration.
- *A collocation scheme* leading to accurate and stable numerical analysis on the boundary has been identified. Our study finds that collocation points corresponding to Greville abscissae lead to more accurate and robust analysis results than those from alternative schemes such as maximum basis, Gaussian quadrature or uniform distribution.
- *Superior convergence rate* of NURBS based BIEM over the usual Lagrange polynomials based BIEM, on a per DOF basis, has been revealed. Our study suggests that the isogeometric analysis via boundary integral obtained using NURBS of order p has the same order of convergence as in Lagrange polynomials of order p based BIEM. This is significant since the convergence rate is independent of inter-element continuity. Thus by leveraging C^{p-1} inter-element continuity, NURBS can converge at the same rate as Lagrange polynomials, but with far fewer DOFs. It is also worth noting that approximating physical fields with B-Spline basis yields nearly identical convergence results as with the rational B-spline basis.
- *Analytical sensitivities* in NURBS based BIEM shape optimization have been derived. They are required in gradient based optimization and other applications such as constructing surrogate models and modeling uncertainties.

2. Isogeometric analysis via boundary integral

In this section we develop the numerical formulation of NURBS based boundary integral for isogeometric analysis. We describe the formulation through an elastostatics problem, although it is readily applicable to other physical problems. For general discussion on BIEM, refer to [15,16].

2.1. Boundary integral for linear elastostatics

The analytical *boundary integral equation* (BIE) [15] for the linear elastostatics problem, in the absence of body force, is formulated as follows:

$$C_{ij}(\mathbf{s})u_j(\mathbf{s}) + \int_\Gamma T^*_{ij}(\mathbf{s},\mathbf{x})u_j(\mathbf{x})\,\mathrm{d}\Gamma(\mathbf{x}) = \int_\Gamma U^*_{ij}(\mathbf{s},\mathbf{x})t_j(\mathbf{x})\,\mathrm{d}\Gamma(\mathbf{x}) \quad (1)$$

where Γ is the structural boundary of domain Ω, $\mathbf{s}$ is the source point (boundary load point), $\mathbf{x}$ is the boundary field point, u_j is the displacement at the field point, t_j is the traction at the field point, U^*_{ij} is the fundamental displacement kernel, T^*_{ij} is the fundamental traction kernel, and C_{ij} is the free term coefficient depending on the boundary geometry at the source point $\mathbf{s}$ [16]. The *fundamental solution* kernels for 2D and 3D problems are given as follows:

$$\begin{aligned}
U^*_{ij}(\mathbf{s},\mathbf{x}) &= \frac{1}{8\pi\mu(1-\nu)}\left[(3-4\nu)\delta_{ij}\ln\frac{1}{r} + r_{,i}r_{,j}\right] \quad (2D)\\
U^*_{ij}(\mathbf{s},\mathbf{x}) &= \frac{1}{16\pi\mu(1-\nu)r}\left[(3-4\nu)\delta_{ij} + r_{,i}r_{,j}\right] \quad (3D)\\
T^*_{ij}(\mathbf{s},\mathbf{x}) &= -\frac{1}{4\pi(1-\nu)r}\left\{\frac{\partial r}{\partial \mathbf{n}}[(1-2\nu)\delta_{ij} + 2r_{,i}r_{,j}]\right.\\
&\quad \left. + (1-2\nu)(n_i r_{,j} - n_j r_{,i})\right\} \quad (2D)\\
T^*_{ij}(\mathbf{s},\mathbf{x}) &= -\frac{1}{8\pi(1-\nu)r^2}\left\{\frac{\partial r}{\partial \mathbf{n}}[(1-2\nu)\delta_{ij} + 3r_{,i}r_{,j}]\right.\\
&\quad \left. + (1-2\nu)(n_i r_{,j} - n_j r_{,i})\right\} \quad (3D)
\end{aligned} \quad (2)$$

where d is the problem dimension ($d = 2$ or 3), $i,j = 1,2,\ldots,d$, $\mathbf{r} = \mathbf{x}-\mathbf{s}$, $r = |\mathbf{r}|$; $r_{,i} = \frac{\partial r}{\partial x_i} = \frac{x_i - s_i}{r}$, n_i is the i-th component of the unit outward normal, δ_{ij} is the Kronecker delta, μ is the shear modulus, ν is Poisson's ratio.

If the above analytical boundary formulation is implemented by discretizing boundary Γ into n_{el} Lagrange elements, then the following discrete form of BIE is obtained:

$$\begin{aligned}
&\mathbf{C}^k(\mathbf{s}^k)\mathbf{u}^k(\mathbf{s}^k) + \sum_{l=1}^{n_{\mathrm{el}}}\left[\int_{\Gamma_l}\mathbf{T}^*(\mathbf{s}^k,\mathbf{x})\mathbf{N}_l\,\mathrm{d}\Gamma(\mathbf{x})\right]\mathbf{u}_l\\
&\quad = \sum_{l=1}^{n_{\mathrm{el}}}\left[\int_{\Gamma_l}\mathbf{U}^*(\mathbf{s}^k,\mathbf{x})\mathbf{N}_l\,\mathrm{d}\Gamma(\mathbf{x})\right]\mathbf{t}_l
\end{aligned} \quad (3)$$

where $k = 1,2,\ldots,n_{\mathrm{nd}}$ and

$$\mathbf{N}_l = \begin{bmatrix} N_1\mathbf{I}_d & N_2\mathbf{I}_d & \cdots & N_{n_{\mathrm{elnd}}}\mathbf{I}_d \end{bmatrix} \quad (4)$$

$\mathbf{s}^k$ is the k-th source point, Γ_l is the l-th Lagrange element. $\mathbf{u}^k$ is the displacement of $\mathbf{s}^k$, n_{nd} is the global node number on boundary Γ, n_{elnd} is the local node number of Γ_l. $\mathbf{N}_l$ is the $d \times (d \times n_{\mathrm{elnd}})$ shape function matrix, $\mathbf{I}_d$ is the $d \times d$ identity matrix. $\mathbf{u}_l$ and $\mathbf{t}_l$ are the $(n_{\mathrm{elnd}} \times d) \times 1$ displacement and traction vectors associated with the n_{elnd} nodes of the boundary element Γ_l.

Collocating source points along the boundary and applying (3) at the collocated points yields equations which could be assembled into the following equation system:

$$[\mathbf{H}]\{\mathbf{u}\} = [\mathbf{G}]\{\mathbf{t}\}. \quad (5)$$

The unknown displacements and tractions could be found by solving the above equation. After all the boundary quantities are known, they are employed to calculate displacement, strain and stress throughout the domain. Due to the interpolatory nature of Lagrange polynomials, all nodes are on the boundary. Thus (5) could be formed by collocating $\mathbf{s}^k$ on all the nodes and applying discrete BIE (3) for each collocated node.

The isogeometric BIEM differs from Lagrange BIEM in that the shape function matrix (4) for the discrete BIE is replaced ($k = 1,2,\ldots,n_{\mathrm{cp}}$) by

$$\mathbf{N}_l = \begin{bmatrix} N_1\mathbf{I}_d & N_2\mathbf{I}_d & \cdots & N_{n_{\mathrm{elcp}}}\mathbf{I}_d \end{bmatrix} \quad (6)$$

where most of the quantities are the same as in (3) except the following differences: n_{cp} is the global control point number on

boundary Γ, n_{elcp} is the local control point number of the l-th element Γ_l. $\mathbf{N}_l$ is the $d \times (d \times n_{\text{elcp}})$ shape function matrix. $\mathbf{u}_l$ and $\mathbf{t}_l$ are the $(n_{\text{elnd}} \times d) \times 1$ displacement and traction vectors associated with the n_{elcp} control points of element Γ_l. The subsequent equation assembly and solving are quite similar to the conventional BIEM. However, the use of NURBS basis function in BIEM does result in a few important changes, which are presented below.

2.2. Collocation

A source point collocation scheme determines the source locations on the boundary where the boundary integral equation (3) is applied. These boundary locations will be referred to as "collocation points" or "source points" interchangeably in this paper. In this paper, we use the NURBS representation with clamped end conditions. We assume that the interpolatory, end control points are chosen as collocation points. A collocation scheme is thus needed to determine the collocation points for the internal control points that are not necessarily located on the boundary. In this paper, we consider four B-spline collocation schemes:

- *Uniform distribution* where the collocation points correspond to a sequence of points that are equally distributed in the parameter domain.
- *Gaussian quadrature* where the collocation points are generated by mapping a number of Gaussian quadrature points from $[-1, 1]$ into the patch parameter domain. Accounting for the end conditions, the number of Gaussian points should be two less than the number of control points in the patch. Note, this scheme is not a pure Gaussian scheme [17] since each curve has two end (i.e. non-Gaussian) points as collocation points.
- *Maximum basis* where the collocation points correspond to the parameters on which one of the shape functions reaches the maximum value [18].
- *Greville abscissae* where the parameters corresponding to collocation points for a degree-p NURBS with $(n + 1)$ control points and a length-$(n + p + 2)$ knot vector $\Xi = \{\xi_0, \xi_1, \ldots, \xi_{n+p+1}\}$ are defined [19,20] by:

$$\zeta_i = \frac{1}{p}(\xi_{i+1} + \xi_{i+2} + \cdots + \xi_{i+p}) \quad i = 0, 1, \ldots, n. \tag{7}$$

The collocation points are generally different under these four collocation schemes. Fig. 1 shows the collocation points from the four schemes for two cubic NURBS curves. Based on our numerical experiments in Section 4.1.4, the Greville abscissa for collocation leads to more accurate and stable analysis and thus is adopted in this paper.

2.3. Singularity evaluation

The fundamental solution kernels in (2) contain terms $\ln\frac{1}{r}$, $\frac{1}{r}$ and $\frac{1}{r^2}$. All these terms tend to infinity as the field point approaches the source point ($r \to 0$), which causes the singularity. The accuracy of singularity evaluation has great influence on the analysis results achieved from equation system (5), since a singular term occurs either in $\mathbf{U}^*$ or $\mathbf{T}^*$, with the former forming the entries of $[\mathbf{G}]$ and the latter forming those of $[\mathbf{H}]$ in (5). The singularities for BIEM fall into two categories: *strong singularity* and *weak singularity* [21], which are treated separately as discussed next.

2.3.1. Strong singularity

Strong singularity arises only in the fundamental traction $\mathbf{T}^*$ for both 2D and 3D cases. It is usually evaluated by an indirect *rigid body motion* method that utilizes a simple fact: a pure translational motion of a finite elastic domain does not result in any shape change of the domain, and hence boundary tractions must be all zeros.

If there are n_{el} elements and n_{collo} collocation points on the boundary, evidently we have $n_{\text{collo}} = n_{\text{nd}}$ (global node number) for Lagrange elements and $n_{\text{collo}} = n_{\text{cp}}$ (global control point number) for NURBS elements. The rigid body motion method sets each entry in $\mathbf{t}_l$ to 0 in (3), thus the global traction vector $\{\mathbf{t}\}$ is a zero vector, which becomes a zero matrix when pre-multiplied by arbitrary compatible matrix (including $[\mathbf{G}]$). Using this fact, an intermediate equation toward obtaining (5) as below:

$$[\hat{\mathbf{C}}]\{\mathbf{u}\} + [\hat{\mathbf{H}}]\{\mathbf{u}\} = \mathbf{O} \Longrightarrow [\hat{\mathbf{C}}] + [\hat{\mathbf{H}}] = \mathbf{O} \tag{8}$$

where $\mathbf{O}$ is a zero matrix, $[\hat{\mathbf{C}}]$ is a sparse matrix where the nonzero entries are related to the strongly singular terms, and the intermediate matrix $[\hat{\mathbf{H}}]$ for obtaining $[\mathbf{H}]$ is assembled as follows:

$$[\hat{\mathbf{H}}] = \mathcal{A}_{\mathbf{T}^*}\left(\int_{\Gamma} \mathbf{T}^*\mathbf{N}\,\mathrm{d}\Gamma\right) \tag{9}$$

where the assembly operator $\mathcal{A}_{\mathbf{T}^*}$ performs integration $\int_{\Gamma_l} \mathbf{T}^*\mathbf{N}\,\mathrm{d}\Gamma$ $(l = 1, \ldots, n_{\text{el}})$ for all the n_{collo} collocation points. We further denote the $d \times d$ block matrix (d: problem dimension) in $[\hat{\mathbf{C}}]$ and $[\hat{\mathbf{H}}]$ by $\hat{\mathbf{C}}_{k,j}$ and $\hat{\mathbf{H}}_{k,j}$, whose rows and columns are associated with the k-th collocation point and the j-th node/control point respectively $(j, k = 1, 2, \ldots, n_{\text{collo}})$.

In the Lagrange BIEM, based on the interpolatory property of Lagrange basis functions, the node(s) with nonzero shape function at the k-th collocation point (k-th node) is the node itself $(j = k)$, the only shape function value being 1. As a result, the rigid body motion method only involves modifying the coefficients on the main diagonal entries of $[\hat{\mathbf{H}}]$ for obtaining $[\mathbf{H}]$, more specifically:

$$\mathbf{H}_{k,k} = \hat{\mathbf{H}}_{k,k} + \hat{\mathbf{C}}_{k,k} = -\sum_{j=1}^{n_{\text{collo}}} \hat{\mathbf{H}}_{k,j} \quad (j \neq k),\ k = 1, \ldots, n_{\text{collo}}.$$

In the rigid body motion implementation for isogeometric BIEM, however, the coefficient modification of $[\hat{\mathbf{H}}]$ are not restricted to diagonal entries since a point on the boundary is defined by up to $p+1$ (or $(p+1) \times (q+1)$) non-zero basis functions and thus by up to $p + 1$ (or $((p + 1) \times (q + 1))$) control points for boundary curves (or surfaces). Suppose the displacements of global control points $\{\mathbf{P}_k\}$ are $\{\mathbf{u}_k\}$ $(k = 1, 2, \ldots, n_{\text{collo}})$. The k-th collocation point $\mathbf{s}^k$ corresponds to Greville abscissae $\boldsymbol{\zeta}^k$, and $\{\chi_i^k\}$ $(i = 1, \ldots, n_{\text{elcp}})$ is the index set of the local control points with nonzero shape functions at $\mathbf{s}^k$. The displacement of the $\mathbf{s}^k$ is then:

$$\mathbf{u}^k = \sum_{i=1}^{n_{\text{elcp}}} N_{\chi_i^k}(\boldsymbol{\zeta}^k)\mathbf{u}_{\chi_i^k}. \tag{10}$$

Substituting (10) into (3) leads to the following rigid body motion formula for the isogeometric BIEM:

$$\begin{aligned} &\mathbf{H}_{\chi_i^k,k} = \hat{\mathbf{H}}_{\chi_i^k,k} + N_{\chi_i^k}(\boldsymbol{\zeta}^k)\hat{\mathbf{C}}_{k,k} \\ &\quad i = 1, \ldots, n_{\text{elcp}},\ k = 1, \ldots, n_{\text{collo}}. \end{aligned} \tag{11}$$

2.3.2. Weak singularity

Weak singularity appears with kernel displacement $\mathbf{U}^*$ when the source point $\mathbf{s}$ is located on the same element as the field point $\mathbf{x}$.

2.3.2.1. 2D weak singularity. The RHS of (3) cannot be accurately evaluated by standard Gaussian quadrature due to the singular kernel U_{ii}^* as $r \to 0$. A common approach is to separate the singular

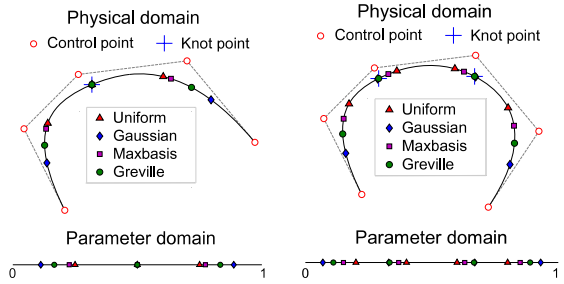

(a) $p = 3$, $n_{cp} = 5$. (b) $p = 3$, $n_{cp} = 6$.

Fig. 1. Four collocation schemes: uniform distribution, Gaussian quadrature, Maximum basis and Greville abscissae, for a degree-p NURBS with n_{cp} control points defined on knot vector Ξ: (a) $\Xi = \{0, 0, 0, 0, \frac{1}{2}, 1, 1, 1, 1\}$; (b) $\Xi = \{0, 0, 0, 0, \frac{1}{3}, \frac{2}{3}, 1, 1, 1, 1\}$. (The first and last collocation points are the two clamped control points and are not shown).

part out of the original weakly singular integrand through a change of variable $\eta = g(\xi)$:

$$f(\xi)\ln\frac{1}{r(\xi)} = f[g^{-1}(\eta)]\ln\frac{1}{\eta\psi(\eta)} = (f\circ g^{-1})(\eta)\ln\frac{1}{\eta} + f(\xi)\ln\frac{1}{(\psi\circ g)(\xi)} \tag{12}$$

where the non-logarithmic part (the 2nd term) contains no singularity and could be well evaluated by standard Gaussian quadrature, while the logarithmic part (the 1st term) could be much more accurately calculated via the logarithmic Gaussian quadrature [15]. The task is then to determine such a parameter transformation g. Assume $r = |\mathbf{x} - \mathbf{s}|$ is the distance between the field point $\mathbf{x}$ and the source point $\mathbf{s}$, which correspond to parameter ξ and ζ respectively. It could be shown that there exists an expression for r:

$$r = |\mathbf{x} - \mathbf{s}| = (\xi - \zeta)\frac{r}{(\xi - \zeta)} \tag{13}$$

such that parameter difference $(\xi - \zeta)$ is singular but the remainder $\frac{r}{(\xi-\zeta)}$ is not. Therefore, the change of variable could simply be $\eta = \xi - \zeta$, and consequently $\psi(\eta) = \frac{r}{\eta}$.

In the Lagrange BIEM, the analytical form of the remainder ψ can be directly obtained [16]. For the isogeometric BIEM, the remainder is obtained by numerically evaluating $\psi = \frac{r}{(\xi-\zeta)}$. Further, η is determined by a generalized change of variable and the formulas are given as follows for three collocation cases

$$\begin{cases} \eta_{\mathbf{x}} = \dfrac{\xi - \xi_L}{\xi_R - \xi_L} & \text{(left-end collocation)} \\ \eta_{\mathbf{x}} = \dfrac{\xi_R - \xi}{\xi_R - \xi_L} & \text{(right-end collocation)} \\ \eta_{\mathbf{x}_1} = \dfrac{\xi - \xi_L}{\xi_I - \xi_L}, \quad \eta_{\mathbf{x}_2} = \dfrac{\xi_R - \xi}{\xi_R - \xi_I} & \text{(mid-side collocation)} \end{cases} \tag{14}$$

where $\xi_{\mathbf{x}}$ corresponds to the field point $\mathbf{x}$, ζ correspond to the source point $\mathbf{s}$; ξ_L, ξ_R are the parameters that correspond to the left and right end of the element respectively, ξ_I is the parameter corresponding to the source point for mid-side collocation, which involves adding two terms from both the left and the right side to $\mathbf{s}$.

The number of Gaussian quadrature points used for the integration within each boundary element is chosen through numerical experiments. The standard quadrature is used for both the non-singular integration and the non-logarithmic part in (12) of the singular integration. The logarithmic quadrature is used only for the logarithmic part in (12). We have chosen 24 points for the non-singular integration, 12 points for the non-logarithmic part of the singular integration and 8 points for the logarithmic part of the singular integration.

2.3.2.2. 3D weak singularity. Weakly singular integrals in 3D are generally handled by the Lachat–Watson transformation [22], in which the singularity is canceled out by an introduced Jacobian term that is also singular, leaving what can be accurately evaluated by the standard Gaussian quadrature. This transformation applies for both Lagrange and NURBS elements.

3. Isogeometric shape optimization via boundary integral

In this section, we describe the formulation of boundary integral based isogeometric shape optimization and detail how to obtain the sensitivities that are needed in gradient-based optimization. For a general introduction on structural optimization, refer to [23,24].

The structural shape optimization problem via the BIEM could be expressed in a nested formulation as below:

$$(\mathbb{SO})_{\text{nf}} \begin{cases} \min\limits_{\boldsymbol{\alpha}} & \hat{f}(\boldsymbol{\alpha}, \mathbf{u}(\boldsymbol{\alpha}), \mathbf{t}(\boldsymbol{\alpha})) \\ \text{s.t.} & \hat{h}_i(\boldsymbol{\alpha}, \mathbf{u}(\boldsymbol{\alpha}), \mathbf{t}(\boldsymbol{\alpha})) = 0, \quad i = 1, \ldots, n_h \\ & \hat{g}_j(\boldsymbol{\alpha}, \mathbf{u}(\boldsymbol{\alpha}), \mathbf{t}(\boldsymbol{\alpha})) \le 0, \quad j = 1, \ldots, n_g \\ & \alpha_k^{\min} \le \alpha_k \le \alpha_k^{\max}, \quad k = 1, \ldots, n_s \end{cases} \tag{15}$$

where the objective $\hat{f} = f(\boldsymbol{\alpha}, \mathbf{u}(\boldsymbol{\alpha}), \mathbf{t}(\boldsymbol{\alpha}))$, equality constraint $\hat{h}_i = h_i(\boldsymbol{\alpha}, \mathbf{u}(\boldsymbol{\alpha}), \mathbf{t}(\boldsymbol{\alpha}))$, and inequality constraint $\hat{g}_j = g_j(\boldsymbol{\alpha}, \mathbf{u}(\boldsymbol{\alpha}), \mathbf{t}(\boldsymbol{\alpha}))$ are functions of design variables $\boldsymbol{\alpha} = \{\alpha_k\}$ $(k = 1, \ldots, n_s)$, with n_s being the number of design variables. The nested formulation means that the state variables, $\mathbf{u}$ and $\mathbf{t}$, are not considered as optimization variables. Rather, they are expressed implicitly as functions of design variables $\boldsymbol{\alpha}$ by the equilibrium equation (5). That is,

$$[\mathbf{H}(\boldsymbol{\alpha})]\{\mathbf{u}(\boldsymbol{\alpha})\} = [\mathbf{G}(\boldsymbol{\alpha})]\{\mathbf{t}(\boldsymbol{\alpha})\}. \tag{16}$$

Example design problems include minimizing the compliance $\int_\Gamma \mathbf{t}^T\mathbf{u}\,d\Gamma$ or nodal displacement $\boldsymbol{u}_i$ under a volume constraint, or a stress constraint $\sigma(\boldsymbol{u}, \boldsymbol{t}) \le \sigma^*$.

The problem $(\mathbb{SO})_{\text{nf}}$ in (15) is in general nonlinear and can be solved by various optimization algorithms. A common approach is gradient-based optimization. In this paper, we use the *method of moving asymptotes* (MMA) [25] as the optimizer and the KKT norm [6] as the convergence criterion.

In gradient-based optimization, sensitivities of how design variables $\boldsymbol{\alpha}$ affect the objective and constraint functions are needed. Analytical sensitivities can be obtained for the discretized BIE. For brevity, we here only outline the main steps for obtaining the discrete analytical sensitivities. Take the function $\hat{f}$ as an example (constraint functions $\hat{h}, \hat{g}$ are handled similarly), differentiation w.r.t. the k-th design variable α_k gives:

$$\frac{\partial\hat{f}}{\partial\alpha_k} = \frac{\partial f}{\partial\alpha_k} + \left(\frac{\partial f}{\partial\mathbf{u}}\right)^T\frac{\partial\mathbf{u}}{\partial\alpha_k} + \left(\frac{\partial f}{\partial\mathbf{t}}\right)^T\frac{\partial\mathbf{t}}{\partial\alpha_k}. \tag{17}$$

From here we will denote $\partial()/\partial\alpha_k$ by a prime $()'$ and drop the component index k of design variable for notation convenience. Usually $\partial f/\partial\alpha_k$, $\partial f/\partial\boldsymbol{u}$ and $\partial f/\partial\boldsymbol{t}$ can be obtained directly from the function f. Obtaining displacement sensitivity $\mathbf{u}'$ and traction sensitivity $\mathbf{t}'$ would require differentiating (16):

$$[\mathbf{H}']\{\mathbf{u}\} + [\mathbf{H}]\{\mathbf{u}'\} = [\mathbf{G}']\{\mathbf{t}\} + [\mathbf{G}]\{\mathbf{t}'\} \tag{18}$$

$[\mathbf{H}']$ is immediately known from $[\hat{\mathbf{H}}']$ by (11) where $[\hat{\mathbf{H}}']$ and $[\mathbf{G}']$ could be found by differentiating the fundamental kernel ($\mathcal{A}_{\mathbf{U}^*}$ is a similar assembly operator as $\mathcal{A}_{\mathbf{T}^*}$ introduced in (9)).

$$\begin{aligned}\hat{\mathbf{H}}' &= \mathcal{A}_{\mathbf{T}^*}\left[\int_\Gamma \mathbf{T}^{*\prime}\mathbf{N}\mathrm{d}\Gamma + \mathbf{T}^*\mathbf{N}(\mathrm{d}\Gamma)'\right]\\ \mathbf{G}' &= \mathcal{A}_{\mathbf{U}^*}\left[\int_\Gamma \mathbf{U}^{*\prime}\mathbf{N}\mathrm{d}\Gamma + \mathbf{U}^*\mathbf{N}(\mathrm{d}\Gamma)'\right].\end{aligned} \tag{19}$$

An exposition of the sensitivity of fundamental solutions, $\mathbf{U}^{*\prime}$ and $\mathbf{T}^{*\prime}$, is available in [26]. We here focus on the geometric sensitivity. We adopt the same global index for $\{\mathbf{P}_k\}$ and $\mathbf{u} = \{\mathbf{u}_k\}$ ($k = 1,\ldots,n_{\mathrm{cp}}$) as given in (10). Now we consider a general source collocation point $\mathbf{s}$ that corresponds to the Greville abscissae $\boldsymbol{\zeta}$ on a NURBS patch, with $\{\chi_i\}$ ($i = 1,\ldots,n^{\mathbf{s}}_{\mathrm{elcp}}$) being the index set of its influential control points (with non-zero corresponding basis functions); similarly, suppose the integration field point $\mathbf{x}$ corresponds to the NURBS patch parameter $\boldsymbol{\xi}$, with the influential control points index being $\{\tau_j\}$ ($j = 1,\ldots,n^{\mathbf{x}}_{\mathrm{elcp}}$). We have the source and the field point sensitivities:

$$\begin{aligned}\mathbf{s}' &= \sum_{i=1}^{n^{\mathbf{s}}_{\mathrm{elcp}}} N_{\chi i}(\boldsymbol{\zeta})P'_{\chi i} = \mathbf{N}^T_\chi \mathbf{P}'_\chi\\ \mathbf{x}' &= \sum_{j=1}^{n^{\mathbf{x}}_{\mathrm{elcp}}} N_{\tau_j}(\boldsymbol{\xi})P'_{\tau_j} = \mathbf{N}^T_\tau \mathbf{P}'_\tau\end{aligned} \tag{20}$$

where $P'_{\chi i}$ and P'_{τ_j} can be directly obtained by propagating the sensitivity from the control point design variables through refinement algorithms [6]. Recall that the distance vector is $\mathbf{r} = \mathbf{x}-\mathbf{s}$ and $\mathbf{r}' = \mathbf{x}'-\mathbf{s}'$. The Jacobian and its sensitivity for 3D problem are found by:

$$\begin{aligned}&\mathbf{J} = \mathbf{x}_{,\xi_1}\times\mathbf{x}_{,\xi_2}\\ &\mathbf{J}' = \mathbf{x}'_{,\xi_1}\times\mathbf{x}_{,\xi_2} + \mathbf{x}_{,\xi_1}\times\mathbf{x}'_{,\xi_2}\\ &\mathbf{x}_{,\xi_1} = \mathbf{N}^T_{\tau,\xi_1}\mathbf{P}_\tau, \qquad \mathbf{x}_{,\xi_2} = \mathbf{N}^T_{\tau,\xi_2}\mathbf{P}_\tau\\ &N_{\tau_j,\xi_l} = \frac{R_{\tau_j,\xi_l}w_{\tau_j}\mathbf{R}^T\mathbf{W} - R_{\tau_j}w_{\tau_j}\mathbf{R}^T_{,\xi_l}\mathbf{W}}{(\mathbf{R}^T\mathbf{W})^2} \quad l = 1,2\end{aligned} \tag{21}$$

where $()_{,\xi}$ denotes the partial derivative w.r.t. ξ. The sensitivity related to Jacobian $\boldsymbol{J}'$ and unit outward normal can then be derived from the above quantities. For more details on NURBS shape sensitivities, refer to [6].

4. Computational examples

In this section, we present numerical results on boundary integral based isogeometric analysis and shape optimization. All numerical results are with the same NURBS basis for both representing geometry and approximating solution space for analysis, unless otherwise noted as in Section 4.1.4.

4.1. Isogeometric analysis

The problem of a square plate with a hole often serves as a benchmark example for examining analysis techniques. We conduct h-, p- and k-refinement to examine the convergence of the isogeometric BIEM.

Fig. 2(a) gives the geometry and boundary conditions of the infinite quarter plate with symmetries w.r.t. both axes, and the constants are: $R = 1, L = 4, E = 10^5, \nu = 0.3, T_x = 10$. The exact traction solution [27,28] evaluated along boundary CD and DE is imposed as the known traction boundary condition for the problem in Fig. 2(b). For imposing the boundary conditions, traction values at control points are assigned to interpolate the exact traction variation. The exact stress at point A is $\sigma_{11}(A) = 30$. Another quantity for comparison is the strain energy where the analytical value is $SE = 0.168898254$. We will use both quantities as a base for comparing the convergence under various refinement schemes.

4.1.1. h-, p-, and k-refinement

The geometry as shown in Fig. 2(b) is represented by 5 quadratic NURBS curves separated by corner points A, B, C, D, E in Fig. 2(b). The quarter circle AB is represented exactly by three control points with weights $1, \frac{1}{\sqrt{2}}, 1$. The 5 curves BC, CD, DE, EA, AB have $2, 2, 2, 2, 1$ elements respectively on the coarsest mesh, and the knot insertion and degree elevation algorithms [29] of NURBS accomplish the h, p, k-refinements. The volumetric analogue of these refinements in isogeometric analysis is available in [2].

The errors of computed $\sigma_{11}(A)$ with respect to the analytical solution, under various refinement schemes, are compared to obtain the convergence results in Fig. 3. During the refinement, the element degree p goes from 2 to 5, and the discretization ratio h/h_0 from 1 (coarsest mesh) to $\frac{1}{10}$ (finest mesh), where h is the characteristic size of the elements at a discretization. Each point on the refinement curves correspond to a pair $(h/h_0, p)$. However, the same pair $(h/h_0, p)$ on the two curves in Fig. 3(a) and (b) could correspond to different element configurations, depending on its the refinement history. More specifically,

- p-refinement in Fig. 3(a) is done by two steps: (1) knot insertion until C^0 inter-element continuity ($P \to Q$); (2) degree elevation ($Q \to R$). This is an analogue of the degree elevation of classical Lagrange elements.
- k-refinement in Fig. 3(b) is achieved by reversing the order of the two refinement algorithms: (1) degree elevation from the coarsest mesh ($K \to L$); and (2) knot insertion ($L \to M$). The C^{p-1} inter-element continuity is preserved.
- h-refinement is obtained via knot insertion. It is used in both p- and k-refinement, such as $P \to Q$ in p-refinement and $K \to N, L \to M$ in k-refinement. The two cases of h-refinements differ in that p-refinement ($P \to Q$) requires repeated h-refinement until C^0 is obtained between elements while k-refinement ($K \to N$) does not.

Although R and M in Fig. 3 have the same degrees $p = 3$ with the same h/h_0, the element configurations, i.e. control points and knot vectors, are different. It is clear that h-, p- and k-refinements all lead to reduced error. Fig. 3(c) overlays the results of p- and k-refinements on the same discretization scale. As data points move leftward along each convergence curve, the element number n_{el} increases as the discretization ratio h/h_0 decreases. The overlaid convergence results show that the NURBS based k-refinement with C^{p-1} inter-element continuity has nearly identical convergence rate as p-refinement with C^0 inter-element continuity on a per element basis. Since C^{p-1} continuity is preserved in k-refinement, for the same number of elements, the number of nodes in k-refined NURBS curves is, in the limit, p times smaller ($p \times q$ times smaller in NURBS surfaces) than the number of nodes in the similarly p-refined mesh.

To better illustrate such nodal advantage of k-refinement, Fig. 4 shows the convergence in Fig. 3(c) on a per DOF ($2\times n_{\mathrm{cp}}$) basis. From the figure, we can see that the accuracy advantage of k refinement over p-refinement becomes more noticeable as the DOF ($2 \times n_{\mathrm{cp}}$)

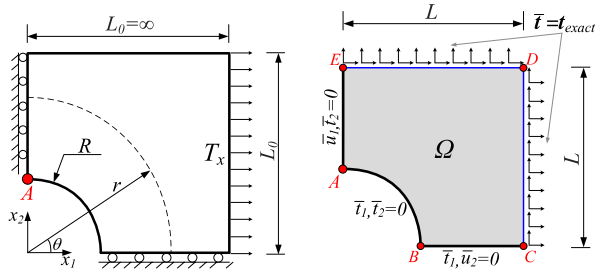

(a) Modeled as an infinite quarter plate.

(b) A finite plate with boundary conditions for BIEM.

Fig. 2. Benchmark example: a square plate with a hole.

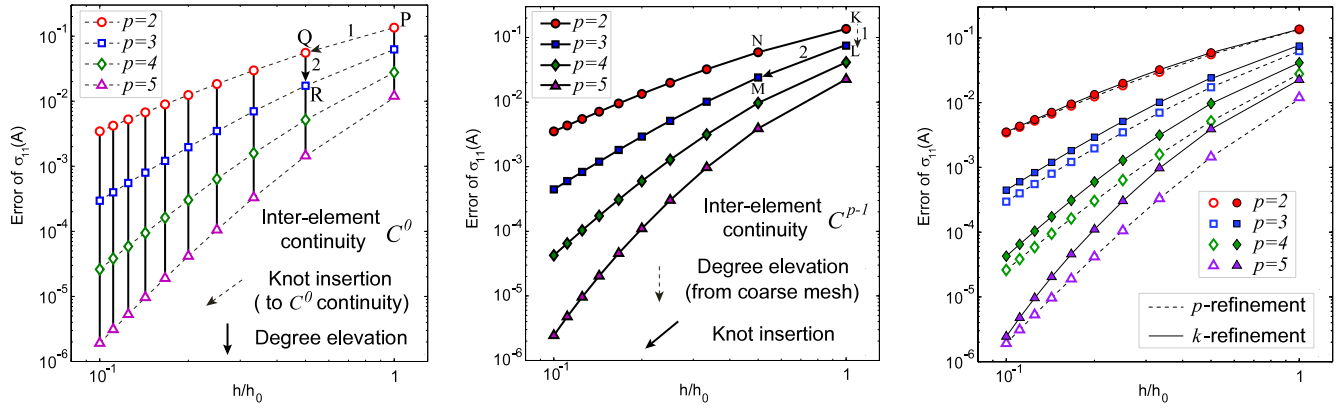

(a) p-refinement.

(b) k-refinement.

(c) Overlay of p-, k-refinement.

Fig. 3. Convergence under p- and k-refinement.

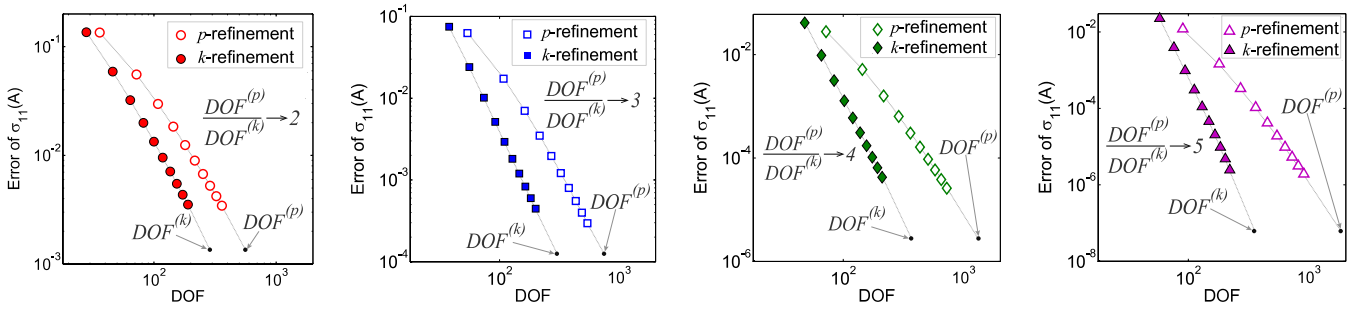

(a) $p=2$.

(b) $p=3$.

(c) $p=4$.

(d) $p=5$.

Fig. 4. Error comparison between p- and k-refinement w.r.t. DOF.

increases and as the element degree is elevated. The slopes at the large DOFs confirm that, as the element number becomes very large, the nodal advantage of k-refinement is approaching p times better than p-refinement.

4.1.2. Lagrange BIEM vs. Isogeometric BIEM

A comparison is also made in Fig. 5 between NURBS based and Lagrange polynomials based BIEM for the example in Fig. 2. Fig. 5(a) shows that, as expected, the p-refinements in NURBS basis and in Lagrange polynomials have almost identical convergence rates. The slight difference can be ascribed to the fact that NURBS uses rational polynomials to represent the exact quarter circle and to approximate the solution space while the other one uses Lagrange polynomials. Fig. 5(b) confirms the nodal advantage of NURBS k-refinement over Lagrange polynomials' p-refinement. Previously we have already established the computational advantage of NURBS k-refinement over NURBS p-refinement on a per-DOF basis, and now we have seen Lagrange p-refinement yields almost the same accuracy with NURBS p-refinement at the same element number and DOF. Therefore NURBS k-refinement has the same computational advantage over Lagrange element on a per-DOF basis.

This study suggests isogeometric analysis via boundary integral obtained using NURBS of order p has the same order of convergence as in Lagrange polynomials of order p based BIEM. Due to the C^{p-1} inter-element continuity in k-refinement, the NURBS based boundary integral is computationally more advantageous over Lagrange polynomials based BIEM on the per DOF basis. This result is similar to what has been reported in computational efficiency of volumetric NURBS based isogeometric analysis and its comparison with Lagrange polynomials based FEA [2].

4.1.3. Lagrange versus NURBS and volumetric versus boundary analysis

Fig. 6 compares four analysis methods from the following combinations: Lagrange versus NURBS and volumetric versus

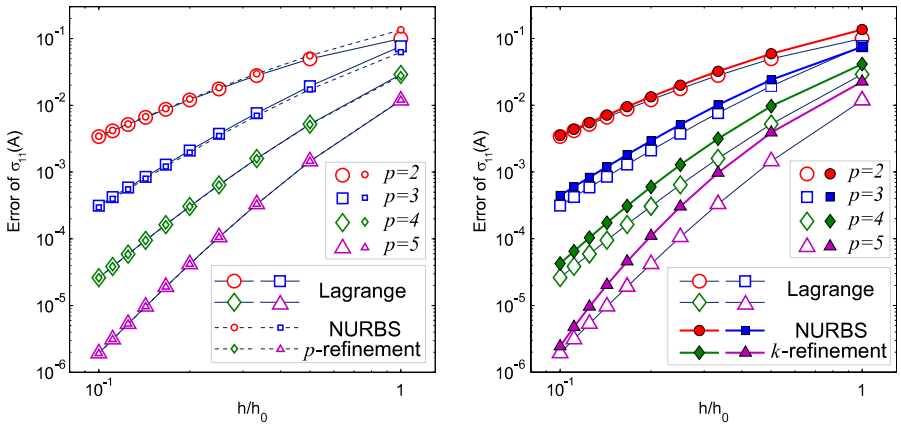

(a) Lagrange and NURBS p-refinement.

(b) Lagrange p-refinement and NURBS k-refinement.

Fig. 5. Comparison of the strain energy error between Lagrange p-refinement and NURBS p-, k-refinement. For p-refinement, Lagrange and NURBS both possess C^0 inter-element continuity, and they have the same DOF at the same degree and same element number. The convergence results of the two are barely distinguishable. The comparison with k-refinement reaffirms the superior efficiency on NURBS based analysis.

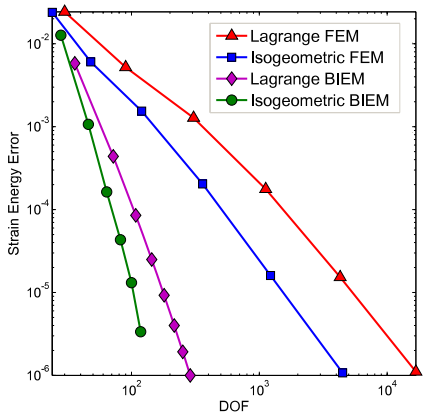

Fig. 6. Strain energy comparison between Lagrange/NURBS and volumetric/boundary analysis, all with quadratic elements.

boundary. The reference quantity now is the strain energy of the problem which has an exact solution [28]. Fig. 6 compares the strain energy error of the four methods all with quadratic elements. We can observe that, on the per DOF basis, (1) isogeometric FEM/BIEM is superior to Lagrange polynomials based FEM/BIEM due to the inter-element continuity and geometric exactness of NURBS, and (2) Boundary integral is better than volumetric FE based analysis on the per DOF basis.

4.1.4. Comparison of collocation schemes

In this paper, we have used the Greville abscissae based collocation scheme and NURBS basis as shape functions for analysis. Here we study how different collocation schemes affect convergence for both elasticity and potential problems. We also compare the convergence when using rational B-splines versus using B-Splines as shape functions for approximating the solution space in analysis. For example, in Fig. 2, weights other than unity are used to represent the quarter circle. When using NURBS, these weights are used in shape functions for approximating the solution space (thus, a nonlinear function space for analysis). When using B-Spline basis, the shape functions in (4) and (11) for analysis are computed with unity weights (thus a linear function space for analysis) but the original weights are retained when computing geometry related quantities such as Jacobian so that the same geometry is used in both CAD model and in analysis.

4.1.4.1. Elasticity problem: plate with a hole. We first compare the convergence result based on the Greville abscissae collocation scheme shown in Fig. 3(b) with results from the three other collocation schemes. The results are shown in Fig. 7 where the error of $\sigma_{11}(A)$ is again measured against the discretization ratio h/h_0. Fig. 8 shows the corresponding condition numbers of the matrices (after reorganizing (5)) for solving the unknowns under various collocation schemes. It can be seen that the maximum basis and Greville abscissae collocation produce reasonably accurate and stable results, with the latter being slightly more accurate. Analysis in the nonlinear function space with the NURBS basis and in the linear function space with B-Spline basis yield almost the same convergence for each collocation scheme.

4.1.4.2. Potential problem: eccentric annulus. We also conducted the comparison for a heat conduction problem in an eccentric annulus. The temperature T on a symmetric eccentric annulus is governed by the Laplace equation $\Delta T = 0$, subject to Dirichlet temperature boundary conditions specified at outer and inner boundaries. The symmetry allows us to model only half the problem as shown in Fig. 9(a), where the two circular boundaries have Dirichlet boundary conditions $T_o = 100$ and $T_i = 0$, and the symmetry lines BC and AD are under Neumann boundary conditions $\frac{\partial T}{\partial \mathbf{n}} = 0$. The boundary geometry for the BIEM is initially represented by 4 NURBS patches separated by 4 corners A, B, C, D, as shown in Fig. 9(b). Fig. 10 shows the convergence of L^2 error norm of temperature along the boundary with respect to mesh size h/h_0 when using the NURBS k-refinement algorithm from degree 2 to 5. Again we see Greville abscissae based collocation outperforms the rest, and NURBS basis and linear B-Spline basis yield nearly identical analysis results.

4.2. Isogeometric shape optimization

In this section, we present two 3D isogeometric shape optimization examples. The convergence criterion is KKT-norm $\leq 10^{-5}$, and the elastic material constants are chosen to be $E = 2 \times 10^5$, $\nu = 0.3$.

4.2.1. Fillet profile

The goal is to find the optimal fillet profile that has the least possible volume without violating the stress constraints. The problem is described in Fig. 11, in which the structure is under tension rightward and the transition profile connecting the two cylinders needs to be found to form the shape of the fillet. The related dimensions are: $L = 20$, $L_1 = 9$, $L_2 = 4.5$, $D_1 = 18$, $D_2 =$

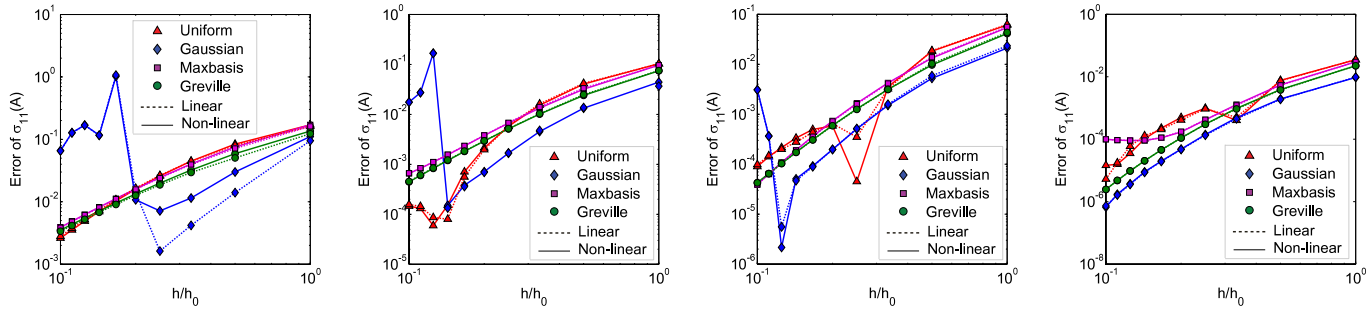

(a) $p = 2$. (b) $p = 3$. (c) $p = 4$. (d) $p = 5$.

Fig. 7. Convergence for elasticity under four collocation schemes.

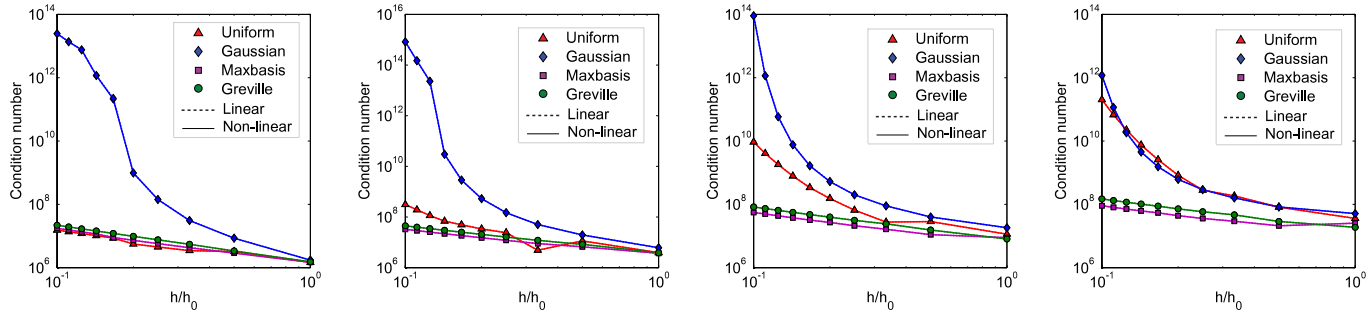

(a) $p = 2$. (b) $p = 3$. (c) $p = 4$. (d) $p = 5$.

Fig. 8. Condition numbers for the study in Fig. 7.

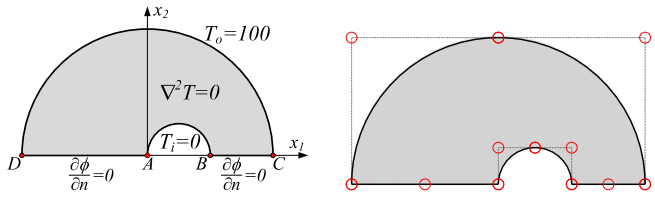

(a) Eccentric annulus (half model). (b) Boundary represented by NURBS.

Fig. 9. Heat conduction in an eccentric annulus.

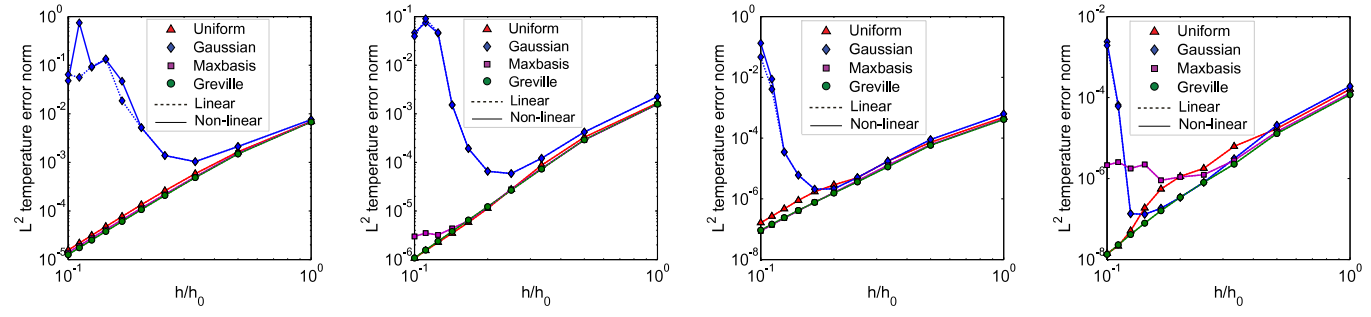

(a) $p = 2$. (b) $p = 3$. (c) $p = 4$. (d) $p = 5$.

Fig. 10. Convergence for heat conduction under four collocation schemes.

9, and the tension is $T_1 = 10$. The allowed von Mises stress on the boundary is $\sigma^* = 12$.

As depicted in Fig. 11, the whole shape is modeled by 36 quadratic elements and 106 control points in 5 patches, which include 2 end circular disks, 2 cylinders and the design patch for the transition portion that connects the two cylindrical surfaces. The design patch is represented by an axisymmetric NURBS patch with 7 control points in the axial direction of the cylinder. The x_1 positions of those control points are not allowed to change; and their x_2 positions can change except the end control points that also lie on the two cylinders, leaving only 5 control points A, B, C, D, E movable. The 5 control positions are controlled by 5 design variables $\alpha_1, \alpha_2, \alpha_3, \alpha_4, \alpha_5$. The design model is refined into 128 elements and 242 control points for analysis as shown in Fig. 12(a). Due to symmetry of the model, we apply the stress constraints only on some stress monitoring points distributed along the x_1 span of the entire model as shown in Fig. 12(a). In the initial design, some of these monitored points, whose x_1 positions are near point E, already violate the stress constraint 12 as shown in Fig. 12(b).

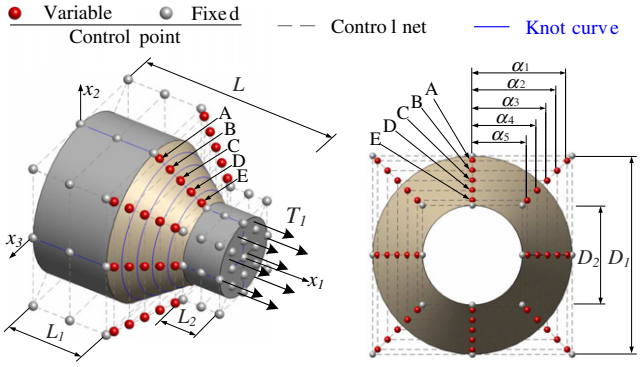

Fig. 11. 3D fillet with load condition and dimensions.

Table 1
Design variable changes in 3D fillet optimization.

Design variable	Lower bound	Upper bound	Initial	Optimized
α_1	4.5	9	8.5500	5.9541
α_2	4.5	9	7.6500	5.0196
α_3	4.5	9	6.7500	4.6504
α_4	4.5	9	5.8500	4.5000
α_5	4.5	9	4.9500	4.5000

The optimized design (Table 1) is obtained after 8 iterations and the optimized fillet shape is shown in Fig. 12(c); the fillet profile matches well with both the intuition and also the shape in [30]. The maximum stress on the boundary has been reduced from 15.4 to 12 as shown in Fig. 12(d).

4.2.2. Connecting rod

The design goal is to find the shape with the minimum volume while satisfying a stress constraint. The full geometry and its loading condition are described in Fig. 13(a), where the connecting rod is symmetric about both $x_1 - x_2$ and $x_2 - x_3$ planes, with the larger hole on the left connecting to the camshaft and the smaller hole on the right connecting to the piston. Here we only consider the static tensile loading case. The piston hole is fully fixed and the left half of the camshaft hole is under a pressure of cosine distribution: $T = T_{\max}|\cos\beta|$, where $T_{\max} = 80$ MPa and $90^\circ \le \beta \le 270^\circ$. The allowed maximum von Mises stress is $\sigma^* = 420$ MPa.

The size and shape of whole model are controlled by 5 parameters in Fig. 13(b); they are: $\alpha_1 = R_3, \alpha_2 = R_4, \alpha_3 = Y_1, \alpha_4 = Y_2, \alpha_5 = Y_3$. The camshaft and piston outer radii R_3, and R_4 control the overall outer shape. The transition profile between the endpoint of the bolt support P_1 and the starting point of the straight platform P_6 is represented by a quadratic NURBS curve of 6 control points $P_1, \ldots, P_6$ on a knot vector $\xi = \{0, 0, 0, \frac{1}{4}, \frac{1}{2}, \frac{3}{4}, 1, 1, 1\}$. P_5 is horizontally aligned with P_6 to ensure a smooth transition onto the straight portion. The x_2 coordinates Y_1, Y_2, Y_3 of the remaining control points P_2, P_3, P_4 are to be optimized. Other constants are $R_1 = 26, R_2 = 10; L_1 = 150, L_2 = 50, L_3 = 120, L_4 = 20, L_5 = 12; R_5 = 7, S_2 = 4.5; S_1 = 10$ and $\theta = 30^\circ$. The x_1 coordinates of the 6 control points are uniformly distributed from L_4 to L_2.

Table 2
Design variables for the connecting rod.

Design variable	Dimension in Fig. 13(b)	Lower bound	Upper bound	Initial	Optimized
α_1	R_3	30	60	34.0000	43.2856
α_2	R_4	15	50	41.4449	15.0000
α_3	Y_1	10	60	41.4449	30.2313
α_4	Y_2	10	60	41.4449	25.1542
α_5	Y_3	10	60	41.4449	20.0771

Only a quarter of the model is analyzed due to the symmetry; the displacement DOFs on the symmetry plane are prohibited: $u_3 = 0$ on $x_1 - x_2$ plane, $u_2 = 0$ on $x_1 - x_3$ plane. The quarter model's boundary is represented by 103 elements and 372 control points in 22 quadratic NURBS patches. The design model is refined into 382 elements and 857 control points for analysis.

The initial NURBS boundary mesh is shown in Fig. 14(a). The side constraints on the 5 design variables are needed to keep the connecting rod in a reasonable shape range, and another shape regularization constraint (the cross product of $P_{i+1}P_i$ and $P_{i+2}P_{i+1}$ should point toward the positive x_3 direction) is applied on the transition NURBS feature to ensure that the profile is curved toward the same direction rather than twisting back and forth. The stress monitoring points in this problem spread over the entire boundary of the quarter model. The analysis mesh is shown in Fig. 14(b). The initial design violates the stress constraint as seen also from Fig. 14(b), where the maximum stress 510 MPa along the camshaft hole exceeds the allowable stress 420 MPa.

The optimized design (Table 2) is obtained after 12 iterations and the resulting shape is shown in Fig. 14(c). The corresponding stress distribution are also shown in Fig. 14(d), which shows that the maximum stress on the boundary has been reduced back to the allowable value 420 MPa.

5. Conclusion

This paper presents a boundary integral based approach to isogeometric analysis and shape optimization where NURBS basis

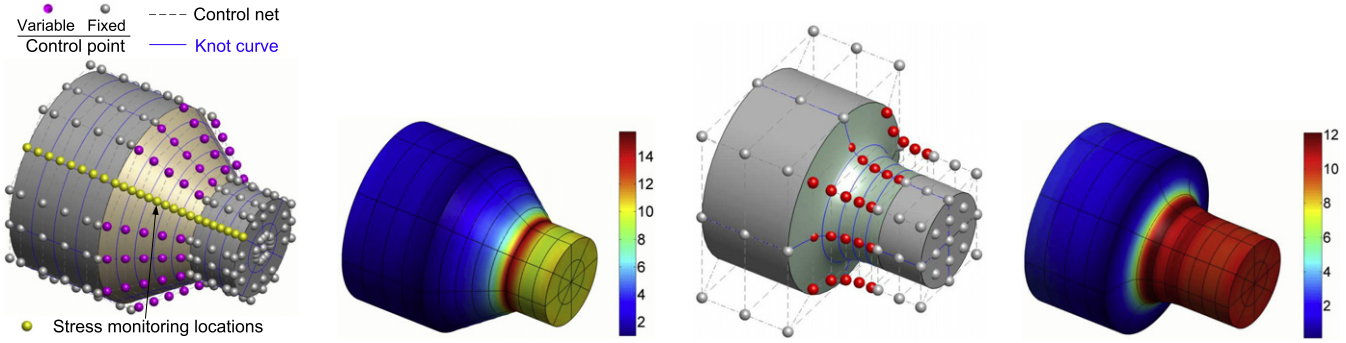

(a) Initial analysis model with 128 quadratic elements and stress monitoring.

(b) Stress before optimization.

(c) Optimized design.

(d) Stress after optimization.

Fig. 12. Initial and optimized fillets.

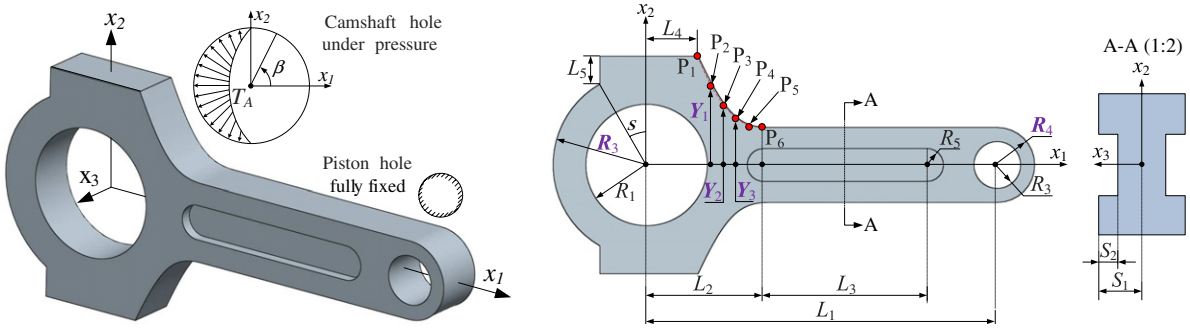

(a) Full model with load conditions.

(b) Geometric dimensions and design variables R_3, R_4, Y_1, Y_2, Y_3.

Fig. 13. 3D connecting rod.

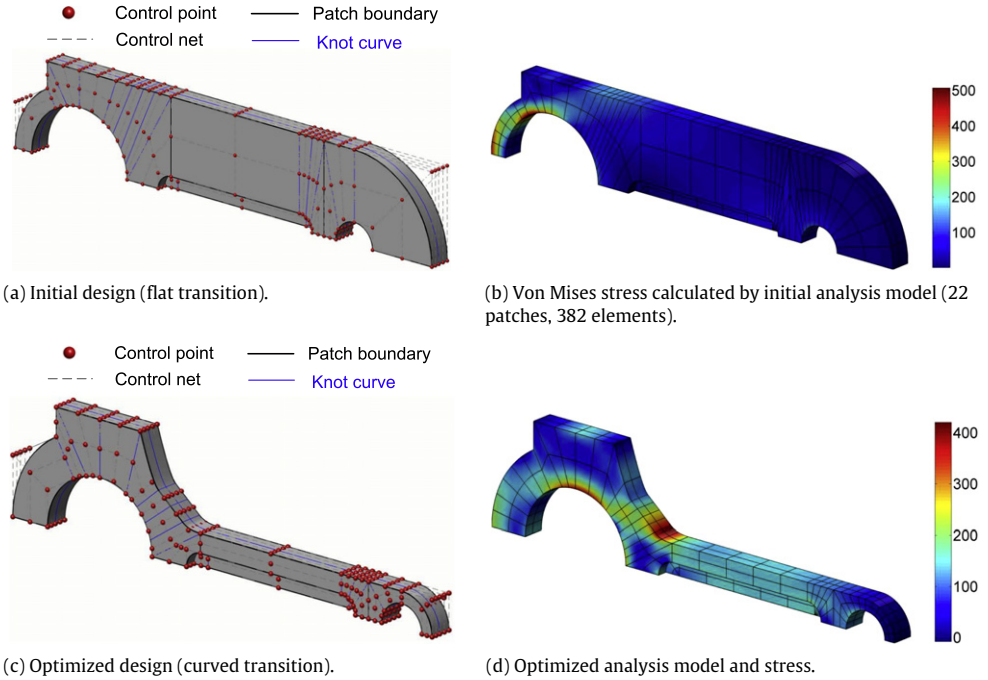

(a) Initial design (flat transition).

(b) Von Mises stress calculated by initial analysis model (22 patches, 382 elements).

(c) Optimized design (curved transition).

(d) Optimized analysis model and stress.

Fig. 14. Initial and optimized rods with stress distribution.

is used to represent the boundary shape and to approximate the physical fields in analysis. This approach has been successfully applied to both elasticity and potential problems. Its application in shape optimization has been demonstrated.

Our study finds that the NURBS based boundary integral method leads to better numerical accuracy on a per-node basis over traditional Lagrange polynomials based BIEM, and over NURBS and Lagrange polynomials based volumetric isogeometric analysis. Approximating the solution space in analysis with *B*-Spline basis and rational *B*-spline basis yield similar analysis results. Collocation points corresponding to Greville abscissae give better numerical accuracy and robustness over other collocation schemes. Due to the use of boundary integral, this approach bypasses the need for domain parameterization which remains a bottleneck in current volumetric integral based isogeometric analysis. This works thus brings us a step closer to the eventual goal of computational design and analysis: seamless integration of design and analysis.

Future work would extend this approach to trimmed NURBS surfaces. One plausible approach would be to convert trimmed NURBS surfaces into *T*-spline surfaces [31], from which boundary integral based isogeometric analysis can be readily developed based on the formulation presented in this paper. Further, NURBS boundaries used in practice may not be perfect where various pieces of boundary curves or surfaces may not fit perfectly due to the imprecisions in modeling, some kind of geometric preprocessing may still be necessary.

Collocation points corresponding to Gauss abscissae do not seem to work well, apparently in contradiction with [17]. This discrepancy will be further investigated in the future.

Acknowledgments

The work is supported in part by NSF grants (#0900170, #1035844 and #1030347). We appreciate reviewers' helpful comments.

References

[1] Hughes TJR, Cottrell JA, Bazilevs Y. Isogeometric analysis: CAD, finite elements, NURBS, exact geometry and mesh refinement. Computer Methods in Applied Mechanics and Engineering 2005;194(39–41):4135–95.
[2] Cottrell JA, Hughes TJR, Bazilevs Y. Isogeometric analysis: toward integration of CAD and FEA. John Wiley and Sons Inc.; 2009.
[3] Wall WA, Frenzel MA, Cyron C. Isogeometric structural shape optimization. Computer Methods in Applied Mechanics and Engineering 2008;197(33–40):2976–88.

[4] Qian X, Sigmund O. Isogeometric shape optimization of photonic crystals via Coons patches. Computer Methods in Applied Mechanics and Engineering 2011;200:2237–55.
[5] Cho S, Ha SH. Isogeometric shape design optimization: exact geometry and enhanced sensitivity. Structural and Multidisciplinary Optimization 2009; 38(1):53–70.
[6] Qian X. Full analytical sensitivities in NURBS based isogeometric shape optimization. Computer Methods in Applied Mechanics and Engineering 2010; 199(29–32):2059–71.
[7] Cohen E, Martin T, Kirby RM, Lyche T, Riesenfeld RF. Analysis-aware modeling: understanding quality considerations in modeling for isogeometric analysis. Computer Methods in Applied Mechanics and Engineering 2010;199(5–8): 334–56.
[8] Yang P, Qian X. A B-spline-based approach to heterogeneous objects design and analysis. Computer-Aided Design 2007;39(2):95–111.
[9] Aigner M, Heinrich C, Jüttler B, Pilgerstorfer E, Simeon B, Vuong A. Swept volume parameterization for isogeometric analysis. In: Mathematics of surfaces XIII. 2009. p. 19–44.
[10] Martin T, Cohen E, Kirby RM. Volumetric parameterization and trivariate B-spline fitting using harmonic functions. Computer Aided Geometric Design 2009;26(6):648–64.
[11] Yang P, Qian X. A general, accurate procedure for calculating molecular interaction force. Journal of Colloid and Interface Science 2009;337(2): 594–605.
[12] Yang P, Qian X. NURBS based molecular force calculation. In: 2009 SIAM/ACM joint conference on geometric and physical modeling. ACM; 2009. p. 361–6.
[13] Politis C, Ginnis AI, Kaklis PD, Belibassakis K, Feurer C. An isogeometric BEM for exterior potential-flow problems in the plane. In: Proceedings of SIAM/ACM joint conference on geometric and physical modeling. 2009.
[14] Cervera E, Trevelyan J. Evolutionary structural optimisation based on boundary representation of NURBS. Part I: 2D algorithms. Computers and Structures 2005;83(23–24):1902–16.
[15] Becker AA. The boundary element method in engineering: a complete course. London (Tokyo): McGraw-Hill; 1992.
[16] Brebbia CA, Dominguez J. Boundary elements: an introductory course. Computational Mechanics Publications; 1992.
[17] De Boor C, Swartz B. Collocation at gauss points. SIAM Journal on Numerical Analysis 1973;10:582–606.
[18] Kwok WY, Moser RD, Jiménez J. A critical evaluation of the resolution properties of B-spline and compact finite difference methods. Journal of Computational Physics 2001;174(2):510–51.
[19] Greville TNE. Introduction to spline functions. Theory and applications of spline functions, 1969. p. 1–35.
[20] Farin G. Curves and surfaces for CAGD. 1993.
[21] Gaul L, Kögl M, Wagner M. Boundary element methods for engineers and scientists: an introductory course with advanced topics. Springer Verlag; 2003.
[22] Lachat JC, Watson JO. Effective numerical treatment of boundary integral equations: a formulation for three-dimensional elastostatics. International Journal for Numerical Methods in Engineering 1976;10(5):991–1005.
[23] Christensen PW, Klarbring A. An introduction to structural optimization. Springer Verlag; 2008.
[24] Haftka RT, Gürdal Z. Elements of structural optimization. Springer; 1992.
[25] Svanberg K. The method of moving asymptotes—a new method for structural optimization. International Journal for Numerical Methods in Engineering 1987;24(2):359–73.
[26] Tai K, Fenner RT. Optimum shape design and positioning of features using the boundary integral equation method. International Journal for Numerical Methods in Engineering 1996;39(12):1985–2003.
[27] Timoshenko SP, Goodier JN. Theory of elasticity. New York: McGraw; 1970.
[28] Zienkiewicz OC, Taylor RL. The finite element method for solid and structural mechanics. Butterworth-Heinemann; 2005.
[29] Piegl LA, Tiller W. The NURBS book. Springer Verlag; 1997.
[30] Shi X, Mukherjee S. Shape optimization in three-dimensional linear elasticity by the boundary contour method. Engineering Analysis with Boundary Elements 1999;23(8):627–37.
[31] Sederberg TW, Finnigan GT, Li X, Lin H, Ipson H. Watertight trimmed NURBS. In: ACM SIGGRAPH 2008 papers. ACM; 2008. p. 1–8.